LAWRENCE
LIVERMORE
NATIONAL
LABORATORY

LLNL-JRNL-410961

A Simultaneous Multi-phase Approach to Determine P-wave and S-wave Attenuation of the Crust and Upper Mantle

M. E. Pasyanos, W. R. Walter, E. M. Matzel

March 2, 2009

Bulletin of the Seismological Society of America

Disclaimer

A simultaneous multi-phase approach to determine P-wave and S-wave attenuation of the crust and upper mantle

Michael E. Pasyanos, William R. Walter, and Eric M. Matzel
Lawrence Livermore National Laboratory, Livermore CA

Submitted to the *Bulletin of the Seismological Society of America*

Corresponding author:

Michael E. Pasyanos
Lawrence Livermore National Laboratory
7000 East Avenue
L-046
P.O. Box 808
Livermore, CA 94551
Tel: (925) 423-6835
FAX: (925) 423-4077
pasyanos1@llnl.gov

Abstract We have generalized the methodology of our regional amplitude tomography from the Lg phase to the four primary regional phases (Pn, Pg, Sn, Lg). Differences in the geometrical spreading, source term, site term, and travel paths are accounted for, while event source parameters such as seismic moment are consistent among phases. In the process, we have developed the first regional attenuation model that uses the amplitudes of four regional phases to determine a comprehensive P-wave and S-wave attenuation model of the crust and upper mantle. When applied to an area encompassing the Middle East, eastern Europe, western Asia, south Asia, and northeast Africa for the 1-2 Hz passband, we find large differences in the attenuation of the lithosphere across the region. The tectonic Tethys collision zone has high attenuation, while stable outlying regions have low attenuation. While crust and mantle Q variations are often consistent, we do find several notable areas where they differ considerably, but are appropriate given the region's tectonic history. Lastly, the relative values of Qp and Qs indicate that scattering Q is likely the dominant source of attenuation in the crust at these frequencies.

Introduction

In a previous study (Pasyanos et al., 2009; PMWR), which this work builds on, we modified the standard regional attenuation tomography technique (e.g. Sereno et al., 1988) to more explicitly define the source expression in terms of an earthquake source model expressed in terms of the seismic moment. We then used thousands of Lg amplitudes in the Middle East to model S-wave crustal attenuation in the frequency band from 0.5 – 10 Hz. We found large variations in the attenuation parameter Q which corresponded well to tectonic processes of the region, most notably tectonic age. We also found that the power-law model of frequency-dependent attenuation might not be the most appropriate parameterization across this frequency band for all regions.

In this study we model the apparent amplitude attenuation of the four main regional phases: Pn, Pg, Sn, and Lg. We consider these phases in their broadest definitions: where Pg and Lg represent P- and S-wave energy traveling in the crust and Pn and Sn represent energy traveling in uppermost mantle lid. In this sense Pg and Lg include both direct rays and crustal reverberations (e.g. PmP and SmS and their multiples). We treat Pn and Sn as turning rays in the mantle lid rather than true head waves based on the observed character of signals. The Pn and Sn signals have similar frequency content to the crustal phases rather than the integrated source spectrum expected for true head waves. In this sense Pn and Sn are represent energy traveling in the lid as a whispering gallery phase or as a multiply reflected turning ray.

We develop the methodology for the multiple regional phase attenuation problem in a similar manner as our previous study for a single phase, by formulating the amplitudes of the four regional amplitudes in terms of a common source moment with differences between phases in the geometrical spreading, path attenuation and site effects. This is very similar to the formulation presented by Walter and Taylor (2001). This methodology allows us to then use the amplitudes of all four phases simultaneously to determine the P and S-wave attenuation of the crust and upper mantle. Here we limit the

scope relative to the previous study by looking at only amplitudes in a single frequency band (1-2 Hz), but the same analysis could readily be extended to other frequency bands or a suite of frequency bands.

Attenuation inversions for each seismic phase are commonly performed separately, but there can be inconsistencies introduced with such an approach. For example, the attenuation for the crustal legs of Pn might be incompatible with the crustal attenuation of Pg amplitudes in the same region. Additionally, source term parameters, such as seismic moment and apparent stress, can be different among the phases for the same event, which is non-physical.

We will first present the methodology by reviewing our previous work and denoting where the technique used here differs. We next examine the new data set of regional phases, amplitude measurements, and the four-phase tomography method. We then discuss our results, focusing on how crust and upper mantle attenuation relate to the tectonic framework of our study area. We will critically compare the crust and upper mantle attenuation, as well as the relative attenuation of P-waves and S-waves. Finally, we will also examine and interpret the source and site terms.

Methodology

The amplitude of seismic phases is controlled by the source excitation S, geometrical spreading G, attenuation B, and site effects P. This is usually represented by the expression:

$$A_{ij} = S_i * G_{ij} * B_{ij} * P_j \qquad (1)$$

where i is the event index and j is the station index. In PMWR, we used this parameterization for Lg amplitudes and defined the earthquake source in terms of seismic moment. Here, we will extend the technique to phases Pn, Pg, and Sn by defining how each of these terms differ from Lg for the other phases. By using both mantle and crustal phases, we can better isolate the distribution of attenuation in the lithosphere. By also using a variety of phases, we can also ensure that moment terms are consistent among the phases, as long as we invert all of the amplitude information simultaneously. We consider each of the terms of equation (1) in turn.

Geometrical spreading term

The geometrical spreading term G_{ij} is represented by a critical distance variable R_o and a spreading variable n (Street et al., 1975). While the parameters for the crustal phases Pg and Lg are expected to be similar, they differ for the upper mantle phases Pn and Sn. The critical distance R_o is set low (1 km) for phases Pn and Sn. Setting the geometrical spreading term correctly is important because both the attenuation term and the geometrical spreading term depend on distance and can trade off with each other. A higher value for the geometrical spreading parameter n requires less anelastic attenuation and hence results in maps of higher Q. Unfortunately, resolving among the two terms is

often somewhat difficult. Sereno et al. (1988) suggest a value of 1.3 for the geometrical spreading of Pn, while the MDAC formulation (Walter and Taylor, 2001) suggests that 1.1 might be a more appropriate value. Taylor et al. (2002) conducted a grid search of parameters and found that 1.3 works best for Pn and 1.1 for Sn in western China. While the absolute values of Q change with variations in n, the relative variation in Q does not, nor does the overall fit to the amplitudes.

A recent study by Yang et al. (2007) considered a more general geometrical spreading for Pn that differs from a classical headwave and is frequency-dependent. These same authors, however, found that this breaks down to a more traditional geometrical spreading as scatterers are introduced. Amplitudes decrease with distance both due to geometrical spreading and attenuation. If the geometrical spreading is too high, it can result in negative values of Q, which are non-physical, as it would increase amplitudes from attenuation alone with distance. We use a value of 1.1 for both Pn and Sn and remind the reader that the absolute value of Q in the mantle is influenced strongly by the choice of geometrical spreading. **Table 1** shows the values of the geometrical spreading terms for each phase.

Source term

As in our previous study, we used the MDAC formulation (Walter and Taylor, 2001) to tie the source term S_i to seismic moment Mo. While the moments are the same in each phase, the P-wave source term S^P differs from the S-wave source term S^S through the radiated energy and, potentially, differing corner frequencies ω_c

$$S^P = F^P M_o/(1+(\omega/\omega_c))^2 \qquad (2)$$

$$S^S = F^S M_o/(1+(\omega/\omega_c))^2 \qquad (3)$$

For convenience, we have set the P-wave and S-wave corner frequencies to be the same: $\omega_c{}^P=\zeta\omega_c{}^S$ (ζ=1) which fixes the ratio between the P-wave source term S^P and S-wave source term S^S, but making the two different ($\zeta\neq1$) simply makes the source term ratio frequency-dependent. With the corner frequencies the same, the ratio of the P-wave and S-wave source terms simply become the ratio of the F terms for P-waves and S-waves.

The F term for P-wave phases (Pn, Pg) and S-wave phases (Sn, Lg) are, respectively:

$$F^P = R^P_{\theta\phi}/4\pi\sqrt{\rho_s\rho_r\alpha_s^5\alpha_r} \qquad (4)$$

$$F^S = R^S_{\theta\phi}/4\pi\sqrt{\rho_s\rho_r\beta_s^5\beta_r} \qquad (5)$$

We use the following values for terms in these equations: $R^p{}_{\theta\phi}$=0.44, $R^s{}_{\theta\phi}$=0.60 (Boore & Boatwright 1984), ρ_s=2700 kg/m^3, ρ_r=2500 kg/m^3, β_s=3500 m/s, β_r=2900 m/s, α_s=6000 m/s, and α_r=5000 m/s. Plugging in these values to equations (4) and (5), we find F^P = 6.83e-17, F^S =4.71e-16, and hence F^S = 6.89 F^P and S^S = 6.89 S^P. We will make

use of this relationship in the inversion, since we only want to solve for one value of the seismic moment parameter for each event.

Site term

The site term P_j, which represents the amplification due to local structure at the station, is similar to the definition in PMWR. The only major difference is that there should be at least two site terms for each station: a P-wave term and an S-wave term. We have considered the question of whether four terms are needed: one for each phase. Since the site term is local near-station effect, however, we have assumed that the site term for Pn and Pg are the same, as are the site terms for Sn and Lg, and use only two site terms, one for P and one for S.

Attenuation term

Obviously, the regional phases Pn, Pg, Sn, and Lg each traverse different paths through the crust and, in case of some phases, the upper mantle. They are, in fact, what define the phases (e.g. Storchak et al., 2003), and the term has to reflect the differing paths. The attenuation term can be generalized as:

$$B_{ij} = \exp\left[-\frac{\omega}{2}\sum_{k=1}^{nlayers}\frac{r_k}{Q_k v_k}\right] \qquad (6)$$

where r is the distance, Q the attenuation parameters, v velocity, and k the layer number.

We have simplified this task by parameterizing the crust and upper mantle as a two layer (true layer over a half-space) model shown in **Table 2**. This makes the problem more straightforward by modeling the attenuation of Pg and Lg as attenuation in the crustal layer and distributing the attenuation of Pn and Sn by a simple raypath through the crust and upper mantle (**Figure 1**).

For Pg and Lg, this becomes:

$$B_{ij} = \exp[\,(-\omega\, r_c) / (2\, Q_c\, v_c)\,] \qquad (7)$$

where r_c, Q_c, and v_c are the crustal distance, attenuation parameter and velocity, respectively. For Pn and Sn, the term becomes:

$$B_{ij} = \exp\left[(-\omega\, r_{c1}) / (2\, Q_{c1}\, v_{c1}) + (-\omega\, r_m) / (2\, Q_m\, v_m) + (-\omega\, r_{c2}) / (2\, Q_{c2}\, v_{c2})\right] \qquad (8)$$

where r_m, Q_m and v_m are the same parameters for the upper mantle, and r_{c1}, r_{c2}, Q_{c1}, Q_{c2}, v_{c2} and v_{c2}, are the parameters for the crustal legs (at the source and station ends) of the phase.

This could be generalized to a many-layer model, although a ray tracer (or equivalent) would have to be employed to determine the specific phase path. Additionally, coverage of the region would have to exceptional in order to resolve the attenuation among the crustal layers. For the moment, while recognizing the limitations, the two layer model can capture a significant portion of the amplitude variation from attenuation.

Inversion

Like PMWR, we invert the amplitude data by taking the base-10 logarithm and correcting for the geometrical spreading term. In addition, since we are combining P-wave and S-wave amplitude information, we need to correct for the difference in the source terms. We can do this either by correcting the P-wave amplitudes (by adding log 6.89 or 0.838) and solving for the S-wave source terms, or by correcting the S-wave amplitudes (by subtracting 0.838) and solving for the P-wave source terms. The approaches are equivalent and either source term can then be solved for the appropriate Mo. Equation (1) becomes for P- and S-wave amplitude:

$$A^P_{ij} = S^P_i * G^P_{ij} * B^P_{ij} * P^P_j \quad (9)$$

and

$$A^S_{ij} = S^S_i * G^S_{ij} * B^S_{ij} * P^S_j = 6.89\, S^P_i * G^S_{ij} * B^S_{ij} * P^S_j \quad (10)$$

In log-space, correcting for geometrical spreading and substituting the source terms and attenuation, for P-wave amplitudes, we get:

$$\log A^P_{ij} - \log G^P_{ij} = \log S^P_i + \log P^P_j - ((\omega \log e)/(2\, Q_{ij}\, v))\, R_{ij} \quad (11)$$

and for S-wave amplitudes, we get:

$$\log A^S_{ij} - \log G^S_{ij} = \log S^S_i + \log P^S_j - ((\omega \log e)/(2\, Q_{ij}\, v))\, R_{ij} \quad (12)$$

which, when substituting the P-wave source term, becomes:

$$\log A^S_{ij} - \log G^S_{ij} - 0.838 = \log S^P_i + \log P^S_j - ((\omega \log e)/(2\, Q_{ij}\, v))\, R_{ij} \quad (13)$$

By equations (11) and (13) we now have a system of equations we can use for the amplitudes of each regional phase which are all functions of Qp and Qs in the crust and upper mantle, the P-wave and S-wave site terms, and a single source term. We then proceed to use amplitude information from Pn, Pg, Sn, and Lg to solve for all attenuation parameters, site terms, and source terms simultaneously. The tradeoffs among the terms of equation (1) are discussed in PWMR.

Data and Tomography

We have started with the dataset from Pasyanos et al. (2009), measuring amplitudes of Pn, Pg, and Sn, in addition to Lg. We then expanded our study area in all directions, but farthest to the north into the Russian Platform, and measured new events at existing stations. Finally, we added stations in the newly expanded region to the north in Russia (OBN, ARU, MHV, PUL), northeast in Kazakhstan and western China (BRVK, MAKZ, WUS, ZAL, KURK), northwest in eastern Europe (KIEV, FINES, MLR, VTS, KWP, SUW), and slightly to the south (PALK, FURI, AAE). We have also "in-filled" the Middle East, by adding data from several temporary deployments, including some stations from the MIDSEA experiment and several PASSCAL deployments in Ethiopia, eastern Turkey, and Pakistan. All-in-all, we have a total of 106 stations.

We use the same signal-to-noise ratio criteria as that from PMWR: a pre-event signal-to-noise ratio of 2.0 and pre-phase signal-to-noise ratio of 1.0. Like the previous study, every waveform is analyst reviewed. If identified, the phase arrival times are picked. Otherwise, theoretical arrival times are used. The theoretical phase velocities vary from region to region depending on the regional structure, but range from 7.9-8.3 km/s for Pn, 5.85-6.3 km/s for Pg, 4.5-4.65 km/s for Sn, and 3.3-3.6 km/s for Lg. Also, it is our general practice to make measurements from several available channels (e.g. BHZ, HHZ, SHZ) from a station in case any one is not available to record a particular event.

We start with a total of 11721 event-station-channel combinations, which is nearly double the overall number we had in PMWR (5889) at 1 Hz. Since we have a larger dataset than our previous study, we can afford to be choosier about our data. Therefore, we have eliminated any events that have only been recorded by a single station, in order to reduce any potential tradeoffs among terms. We also only use one channel for any given event – station path. After eliminating these, we have 10020 event-station paths with picks (**Figure 2**).

Of the four regional phases, we have the most phases for Pn (8178). We have fewer phases for Sn (6554) which, not being a first-arriving phase, has a lower signal-to-noise ratio. Sn is also blocked in particular regions like eastern Turkey (Gök et al., 2000). We also have fewer phases for Lg (6353) which can propagate to longer distances than Pn and Sn, but suffers from phase blockage in certain regions, notably oceanic regions and other regions where the crust thins (Zhang and Lay, 1995). Lastly, we have significantly fewer paths for Pg (5567) which does not propagate to longer distances as well as Lg.

In all cases, however, we have somewhat similar coverage of our study area (**Figure 3**). All phases have excellent coverage of a wide swath encapsulating the Tethys Belt and extending down the Red Sea and Gulf of Aden to include Arabia. The Indian subcontinent is only sparsely covered to the northwest. We have significantly poorer coverage in Russia, northeast Africa, and the oceanic regions, where a lack of seismicity results in significantly fewer paths recording regional phases. Blanketing the region with amplitude measurements is necessary in this region because of the large amplitude changes we see over short distances. For example, **Figure 4** shows large changes in Lg amplitudes recorded at station MALT between a southern group which crosses the

Arabian Platform and a northern group in which propagation stays within the Turkish Plateau. The northern group has much smaller Lg amplitudes than the southern group.

The next step in the inversion is to populate the initial values of Q, S, and P in the inversion. The source term S_i is set to the appropriate value for the moment and phase (**equations 2 and 3**). Moments are either taken from available catalogs, estimated from regional waveform modeling, or derived from coda waves. Where these options are not available, moments are estimated from other magnitudes. The site term P_j for both P-waves and S-waves is initialized to 1.0.

For starting values of Qs and Qp in the crust, we set terms S and P and solved for the best 1-D value using Lg only and Pg only, respectively. We then used these values in the crust and solve for the best values of Q in the mantle using Sn and Pn. We find a starting value of Qp = 300 and Qs = 300 for the crust and Qp = 800 and Qs = 400 for the upper mantle. We note that in the crust, these values differ significantly from the relationships often used to relate Qp and Qs (e.g. Qp = (9/4) Qs (derived from Anderson and Hart, 1978 where vp/vs = √3); Qp = 1.5 Qs (Olsen et al., 2003)). This could, in part, be due to the fact that we are solving for apparent attenuation (which is a combination of intrinsic and scattering attenuation) and not simply intrinsic attenuation alone, where we might expect these relations to hold.

We have gridded our study area into 0.5º blocks. A Laplacian function smoothes Q variation within the crust and upper mantle, but there is no additional constraint between the attenuation of the crust and upper mantle. A conjugate gradient solver is then used on the combined series of equations. We solve for a total of seven sets of parameters: 1) crustal Qs, 2) upper mantle Qs, 3) crustal Qp, 4) upper mantle Qp, 5) S-wave site terms, 6) P-wave site terms, and 7) source terms.

Results

In running the inversion, one of our first tests was in comparing crustal Qs, determined from Lg phases only to the crustal Qs using all phases. The results are almost identical. We performed similar tests for crustal Qp derived from Pg amplitude data, as well, before running the full four-phase inversion. Overall variance reduction is high. Initial misfit of the data is about 0.884 log-amplitude units, with slightly higher misfit (~1.1) for the Lg phase. After inversion, this misfit is reduced to 0.319 log-amplitude, and the misfit is approximately the same for all the phases. Results of the inversion for the attenuation parameter Q are shown in **Figure 5**. Panels show the following: a) crustal Qs; b) upper mantle Qs; c) crustal Qp; and d) upper mantle Qp.

The crustal Qs maps (**Figure 5a**) look similar to the results we found in Pasyanos et al. (2009). While this map is primarily derived from the amplitudes of Lg phases, it also includes the crustal legs of Sn. The addition of data to the north enhances and better isolates the lateral variation of the low-attenuation region (Kazakh Platform) suggested in the first study. More amplitude measurements in the subcontinent does not extend the region of high Q further southeast. The addition of crustal legs from the Sn phase does

not seem to have altered the pattern of attenuation anomalies significantly from the previous study.

The attenuation is high (low Q) in the Turkish-Iranian Plateau and the Zagros Mts., with the highest attenuation found in eastern Turkey (Q = 100-200). We find moderate attenuation (average Q) along the Red Sea and Arabian Platform, and low attenuation (high Q) in the Arabian Shield, Tajik Basin, and Indian Shield. Overall, the mean Qs in the crust is 307 and the range (determined by the mean plus and minus two standard deviations in log space) is 174-541.

Figure 5b shows upper mantle Qs, which is derived exclusively from Sn amplitudes. The mean and range in this case is 452 and 169-1210. It is important to keep in mind that phases such as Sn and Pn sample the upper mantle lid (at least where it exists) and is not necessarily representative of the rest of the upper mantle. We find high attenuation along the Red Sea, Arabian Shield, the Zagros Mts., and the Turkish-Iranian Plateau. It appears particularly high in eastern Turkey and at the Afar Triple Junction. We find low attenuation in the eastern Arabian Platform, Tajik Basin, northern India and Pakistan. Outside of the rift zones, there tends to be low attenuation in regions of oceanic crust, including the eastern Mediterranean, South Caspian and, to a lesser extent, the Black Sea. If we compare to the Sn efficiency maps of Gok et al. (2003) and Al-Damegh et al. (2004), we see a remarkable similarity.

Crustal Qp is shown in **Figure 5c**. This map is mainly derived from the amplitudes of Pg phases, but also include the crustal legs of Pn. We find a mean of 338 with a range of 206-554. The attenuation is high along the Red Sea, the Turkish Plateau, and much of the Iranian Plateau. Like crustal Qs, we still see low attenuation in the Tajik Basin, Indian Shield, and northern Arabian Platform, but it isn't as strong in the Indian Shield and Arabian Platform/Shield. The Makran differs from the Iranian Plateau to the north. Unlike mantle Qs, we find a wide swath of high attenuation extending from the Red Sea east into the Arabian Shield.

The last panel (**Figure 5d**) shows upper mantle Qp, which is derived exclusively from Pn amplitudes. The mean and range of mantle Qp is 1098 and 193-6228. This parameter is significantly higher and has a wider range than crustal Qp (~350). Like Sn, Pn samples the upper mantle lid and, therefore, we are sensitive to attenuation at these depths. We see high attenuation running from a ridge along the Red Sea and Dead Sea Rift east into western Arabia. We also find high attenuation under the Turkish Plateau and, to a lesser extent, the Iranian Plateau. With better coverage of the area from Pn, we can start to see differences between the attenuation of Phanerozoic Western Europe and the Precambrian Eastern European Platform along the Trans-European Suture Zone. Attenuation is low in eastern Arabian, the eastern Mediterranean, and the southern Caspian. The patterns of anomalies resemble those of mantle Qs, but there appear to be some large differences between mantle Qp and Qs in northern Arabia. Values of Q compare favorably to the results of Morozov et al. (1998) who find Qp ~ 1500 at shallow upper mantle depth under the Russian Platform and Siberia.

We summarize the average and range of attenuation in our study area in **Table 3**. If we compare our results to the teleseismic body wave study of Der et al. (1986), they find in the EURS Q model of the Eurasian Shield at 1.0 Hz 365-445 for Qs and 800-1000 for Qp in the crust, and 200-263 for Qs and 450-800 for Qp in the mantle lid and low velocity zone. In general our Qs is within their range or lower than these results, but that is not unexpected when comparing the tectonic Tethys Belt to a lower attenuation shield region. However, we find a lower Qp in the crust and higher Qp in the mantle than the EURS model with the assumed Qp=(9/4)Qs relation. Differences in the upper mantle could also be due, in part, to the depth sensitivity of the two methods. Our method is primarily sensitive to the lid, while t* studies are more sensitive to bulk attenuation. Also, keep in mind on any direct comparisons of Q the large tradeoff between the values of Q and the geometrical spreading.

Using the inversion results, we can take a cross-section through any arbitrary slice of our crust and upper mantle attenuation model. Perhaps one of the most interesting profiles is one spanning from the African Platform, across the Arabian Peninsula and the Zagros Mts., into the Iranian Plateau. This cross-section (shown in **Figure 6**) highlights one of the key observations of this study, which is that in some regions there are large differences in the relative attenuation of the crust and mantle. What we find is that, while the high crustal attenuation in the Red Sea is fairly spatially limited, it is spread to the northeast under the Arabian Shield in the mantle. This is consistent with low Pn and Sn velocities found under this region (e.g. Ritzwoller et al., 2002). Furthermore, we find very high Q under the Arabian Platform, where the lithosphere is thick (Hansen et al., 2007). To the southwest, the moderate attenuation of the African Platform is expected given the thinner lithospheric thickness of the Saharan meta-craton (Pasyanos and Nyblade, 2007). To the northeast, the high Q is terminated by the Zagros Mts. in the crust, and the Iranian Plateau in the mantle.

In addition to lateral attenuation, we also invert for site and source terms. Using **equations (2) and (3)**, we can interpret the source terms as changes to the seismic moment. Moment terms are somewhat more constrained than our previous study. In PMWR, it was possible to have events recorded by a single station and, hence, there was more non-uniqueness in how much of the amplitude was affected by site term changes or attenuation changes along path. Constraints in that case came from other paths traversing the same region. With several phases recording an event having appropriate source terms for a given moment, there is less ambiguity in the distribution of amplitude effects. **Figure 7** shows a comparison of the moment derived from the inverted source term compared to our original moment estimates. The RMS difference between the two is about 0.146 magnitude units, which is significantly less than the 0.209 m.u. RMS that we found in PMWR. Like that study, we find that true moments vary less in the inversion than moments derived from other magnitude estimates.

The S-wave and P-wave site terms we display on a map (**Figure 8a and 8b**). The standard deviation of site terms is 0.36 in log-amplitude for S, and 0.28 for P. Several things are observed. First, site terms tend to be higher in shields and platforms and lower in tectonic regions. Beyond this general trend, however, there is variability over small

scales. It appears that P-wave and S-wave site terms are somewhat correlated. When we directly compare the P-wave site terms to the S-wave site terms (**Figure 8c**), we find that they show some similarities, but not overwhelmingly so. The correlation parameter between the two is 0.41 which has some correlation, but not a very strong one. This justifies the use of separate site terms for P and S.

Returning to attenuation, the last things we compare are the ratios of Qp/Qs for the crust and upper mantle (**Figure 9**). Only points having more than a minimum number of hits are plotted. The correlations here are surprisingly weak given the similarity of some of the maps in **Figure 5**. It does not appear that relations such as Qp = (9/4)Qs characterize the relation between the observed P-wave and S-wave attenuation. For the crust, neither Qp nor Qs is systematically larger, although it does appear that Qp is usually greater than Qs in the mantle. When scattering dominates over intrinsic friction, the compressional and shear wave quality factors are approximately equal (Richards and Menke, 1983). It appears then that scattering Q might play a larger role in crustal attenuation, particularly in regions like shields where the intrinsic attenuation is low.

Conclusions

Making use of a new attenuation formulation which explicitly defines the source expression in terms of seismic moment, we use the amplitudes of regional phases Pn, Pg, Sn, and Lg to determine the seismic attenuation of the lithosphere across our study area. By taking advantage of the differing sampling of the earth for the four phases, we can isolate the P-wave and S-wave attenuation of the crust and upper mantle, while consistently accounting for source and site effects.

What we find are patterns in the attenuation maps that relate to the overall tectonic activity of the region. What is most clearly indicated is that thermal altering of the crust and upper mantle increases seismic attenuation. For example, ridges, orogenic zones and high plateaus being thermally supported have high crustal attenuation. Nearby, undisturbed shields and platforms have low crustal attenuation. In the mantle, we find that regions with well-developed mantle lids have low attenuation, while regions with recent and ongoing tectonic activity have high mantle attenuation. While undisturbed shields and platforms have high Q in both the crust and mantle, those with more recent mantle activity see significant differences between them.

On average, we find that values of mantle Q are higher than crustal Q for both Qp and Qs. However, large variations in this parameter from region to region make this a far from universal feature. Whereas in the crust both Qp and Qs generally range from 200-500, in the mantle Qs has about the same range, but Qp ranges from 200-2000. Surprisingly, we also find that values of P-wave attenuation and S-wave attenuation are somewhat comparable, particularly in the crust, which may indicate that scattering Q (which is probably on the same order for P and S) is a larger component of total Q than intrinsic Q, which we would expect to be higher for compressional waves.

In order to demonstrate the technique, we have made a number of approximations. Future work could focus on making more exact path calculations. For example, we could add more crustal (and upper mantle) layers and employ a better ray tracer. Similarly, we could put in variable crustal velocity and crustal thickness. We can implement these improvements as regional amplitude data increases enough to justify them.

Data and Resources

Most of the seismograms data used in this study can be obtained from the Incorporated Research Institutes in Seismology (IRIS) Data Management Center (DMC) at www.iris.edu, the U.S. National Data Center (USNDC) at www.tt.aftac.gov, GEOSCOPE at geoscope.ipgp.jussieu.fr, IIEES at www.iiees.ac.ir, GEOFON at geofon.gfz-potsdam.de, and MEDNET at mednet.rm.ingv.it. Other data was obtained directly from networks in Azerbaijan, Georgia, Israel, Jordan, Kazakhstan, Kuwait, Oman, Saudi Arabia, Turkey, and United Arab Emirates. Plots were made using the Generic Mapping Tools (GMT) version 4.2.0 (Wessel and Smith, 1998; www.soest.hawaii.edu/gmt).

Acknowledgments

We thank Doug Dodge and Mike Ganzberger for the Regional Body-wave Amplitude Processor (RBAP) tool, Stan Ruppert and Terri Hauk for maintaining our seismic database, and Flori Ryall for her regional picks. This work was performed under the auspices of the U.S. Department of Energy by Lawrence Livermore National Laboratory under Contract DE-AC52-07NA27344. This is LLNL contribution LLNL-JRNL-******.

References

Al-Damegh, K., E. Sandvol, A. Al-Lazki, and M. Barazangi (2004). Regional seismic wave propagation (Lg and Sn) and Pn attenuation in the Arabian Plate and surrounding regions, *Geophys. J. Int.*, **157,** 775-795, doi:10.1111/j.1365-246X.2004.02246.x.

Anderson, D.L. and R.S. Hart (1978). Q of the earth, *J. Geophys. Res*., **83**, 5869-5882.

Bird, P., 2003. An updated digital model of plate boundaries, *Geochem. Geophys. Geosyst.,* **4**, 1027, doi:10.1029/2001GC000252.

Boore, D.M. and J. Boatwright (1984). Average body-wave radiation coefficients, *Bull. Seism. Soc. Amer.*, **74,** 1615-1621.

Der, Z.A., A.C. Lees, and V.F. Cormier (1986). Frequency dependence of Q in the mantle underlying the shield areas of Eurasia, Part II: The Q model, *Geophys. J. R. astr. Soc.*, **87**, 1103-1112.

Gök, R., N. Turkelli, E. Sandvol, D. Seber, and M. Barazangi (2000). Regional wave propagation in Turkey and surrounding regions, *Geophys. Res. Lett.*, **27,** 429-432.

Gök, R., E. Sandvol, N. Turkelli, D. Seber, and M. Barazangi (2003). Sn attenuation in the Anatolian and Iranian plateau and surrounding regions, *Geophys. Res. Lett.*, **30**, 8042, doi:10.1029/2003GL018020.

Hansen, S.E., A.J. Rodgers, S.Y. Schwartz, and A.M.S. Al-Amri (2007). Imaging ruptured lithosphere beneath the Red Sea and Arabian Peninsula, *Earth. Planet. Sci. Lett.*, **259**, 256-265, doi:10.1016/j.epsl.2007.04.035.

Laske, G., and G. Masters (1997). A global digital map of sediment thickness, *EOS Trans. AGU*, **78**, F483.

Morozov, I.B., E.A. Morozova, S.B. Smithson, and L.N. Solodilov (1998). 2-D image of seismic attenuation beneath the Deep Seismic Sounding profile "Quartz", Russia, *Pure Appl. Geophys.*, **153**, 311-343.

Olsen, K.B., S.M. Day, and C.R. Bradley (2003). Estimation of Q for long-period (2 sec) waves in the Los Angeles Basin, *Bull. Seism. Soc. Am.,* **93**, 627–638.

Pasyanos, M.E. and A.A. Nyblade (2007). A top to bottom lithospheric study of Africa and Arabia, *Tectonophys.*, **444**, 27-44, doi:10.1016/j.tecto.2007.07.008.

Pasyanos, M.E., W.R. Walter, M.P Flanagan, P. Goldstein, and J. Bhattacharyya (2004). Building and testing an *a priori* geophysical model for Western Eurasia and North Africa, *Pure Appl. Geophys.*, 161, 235-281.

Pasyanos, M.E., E.M. Matzel, W.R. Walter, and A.J. Rodgers (2009). Broadband Lg attenuation modeling in the Middle East, in press *Geophys. J. Int.*

Pasyanos, M.E. (2009). Lithospheric thickness modeled from long period surface wave dispersion, submitted to Tectonophysics.

Richards, P.G. and W. Menke (1983). The apparent attenuation of a scattering medium, *Bull. Seism. Soc. Amer.,* **73**, 1005-1021.

Ritzwoller, M.H., M.P. Barmin, A. Villaseñor, A.L. Levshin, and E.R. Engdahl (2002). Pn and Sn tomography across Eurasia to improve regional seismic event locations, *Tectonophys.*, **358**, 39-55.

Romanowicz, B. and B.J. Mitchell (2007). Deep earth structure – Q of the earth from crust to core, *Treatise on Geophysics*, **1**, 731-774, doi:10.1016/B978-044452748-6.00024-9. (not currently referenced)

Sereno, T.J., S.R. Bratt, and T.C. Bache (1988). Simultaneous inversion of regional wave spectra for attenuation and seismic moment in Scandinavia, *J. Geophys. Res.,* **93**, 2019–2036.

Storchak, D.A., J. Schweitzer, and P. Borman (2003). The IASPEI standard seismic phase list, *Seism. Res. Lett.*, **74**, 761-771.

Street, R.L., R. Herrmann, and O. Nuttli (1975). Spectral characteristics of the Lg wave generated by central United States earthquakes, *Geophys. J. R. Astron. Soc.*, **41,** 51-63.

Taylor, S.R., A.A. Velasco, H.E. Hartse, W.S. Phillips, W.R. Walter, and A.J. Rodgers (2002). Amplitude corrections for regional seismic discriminants, *Pure Appl. Geophys.*, **159**, 623-650.

Walter, W.R. and S.R. Taylor (2001). A revised magnitude and distance amplitude correction (MDAC2) procedure for regional seismic discriminants: theory and testing at NTS, Lawrence Livermore National Laboratory, UCRL-ID-146882 http://www.llnl.gov/tid/lof/documents/pdf/240563.pdf

Wessel, P. and W.H.F. Smith (1998). New, improved version of Generic Mapping Tools released, *EOS trans. AGU,* **79,** 579.

Yang, X., T. Lay, X.-B. Xie, and M.S. Thorne (2007). Geometric spreading of Pn and Sn in a spherical earth model, *Bull. Seism. Soc. Amer.*, **97**, 2053-2065, doi:10.1785/0120070031.

Zhang, T.R. and T. Lay (1995). Why the Lg phase does not traverse oceanic crust, *Bull. Seism. Soc. Amer.*, **85**, 1665-1678.

Lawrence Livermore National Laboratory
7000 East Avenue
L-046
P.O. Box 808
Livermore, CA 94551
(M.E.P., W.R.W., E.M.M.)

Tables

Table 1. Geometrical spreading term parameters used for each phase.

phase	n	R_o (km)
Pg, Lg	0.5	100
Pn, Sn	1.1	1

Table 2. Velocity model used.

Layer	Depth (km)	Vp (km/s)	Vs (km/s)
Crust	0 - 30	6.50	3.70
Upper mantle	30 -	8.00	4.50

Table 3. Mean and 2 standard deviation range of Q from this study.

	P-wave	S-wave
Crust	338 (206-554)	307 (174-541)
Upper mantle	1098 (193-6228)	452 (169-1210)

Figure captions

Figure 1. Schematic diagram of regional phases Pn (cyan), Pg (green), Sn (dashed red), and Lg (dashed magenta) and how they sample the velocity and attenuation structure of the crust and upper mantle.

Figure 2. Number of Pn, Pg, Sn, and Lg measurements (yellow), paths (green), and events (blue) passing the signal-to-noise criteria. The measurements are recorded on 107 stations.

Figure 3. Path map of Pn, Pg, Sn, Lg attenuation measurements in our study area. Stations are shown by yellow triangles, events by black circles, and paths by cyan lines (Pn), green lines (Pg), red lines (Sn) and magenta lines (Lg).

Figure 4. Waveforms for two sets of events recorded at station MALT (Malatya, Turkey) separated into a northern group (which crosses the Turkish Plateau) and a southern group (which crosses the Arabian Platform). All traces have been filtered between 1.0 and 2.0 Hz. The approximate arrival of the Lg phase (3.4 km/s) is highlighted in red. Inset shows the locations of the northern group (red circles), southern group (blue circles), and recording station (yellow triangle).

Figure 5. Maps of the attenuation quality factor Q for a) shear-wave attenuation in the crust (crustal Qs), b) shear-wave attenuation in the mantle (mantle Qs), c) compressional-wave attenuation in the crust (crustal Qp), and d) compressional-wave attenuation in the mantle (mantle Qp). Dark lines indicate plate boundaries from Bird (2003).

Figure 6. Cross-section from Africa (A) extending northwest across the Arabian Peninsula into Iran (B). The cross-section shows the shear-wave attenuation factor in the crust and mantle along the profile. Solid lines in the profile represent, with increasing depth, basement depth (from Laske and Masters, 1997), Moho depth (modified from Pasyanos et al., 2004), and LAB depth (Pasyanos, 2009). Dashed line is the 30 km depth.

Figure 7. Plot showing a comparison of the inverted moment magnitudes to original moment magnitude estimates. Symbols indicate either moment estimates (blue circles) or converted magnitude estimates (red inverted triangles).

Figure 8. Site term maps showing a) the P-wave source term, and b) the S-wave source term. c) A comparison of the P-wave and S-wave site terms.

Figure 9. A comparison of Qp and Qs for a) the crust and b) the mantle. The solid line shows Qp = Qs, while the dashed line indicates Qp = (9/4) Qs. Initial values used in the inversion are shown by the green circles.

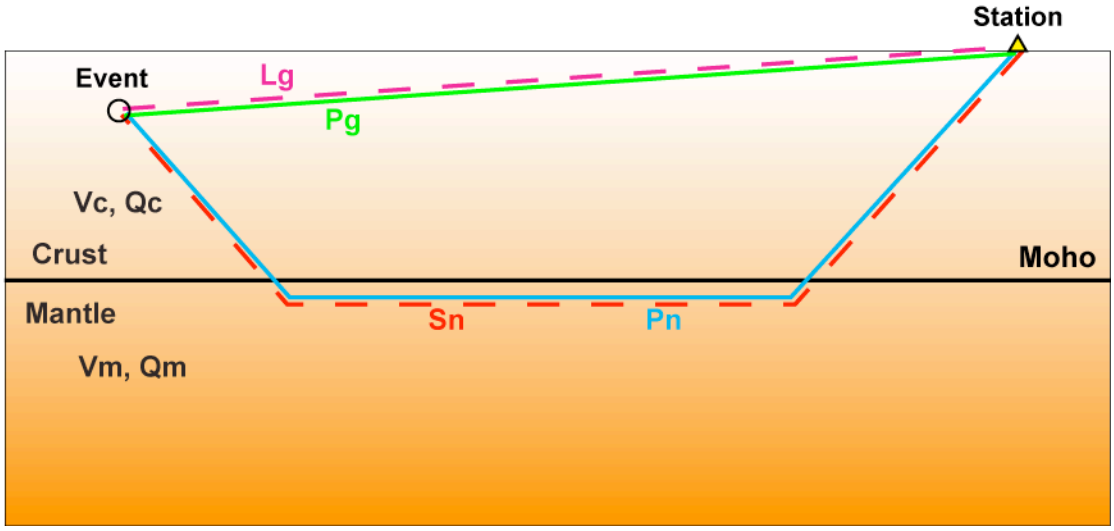

Figure 1.

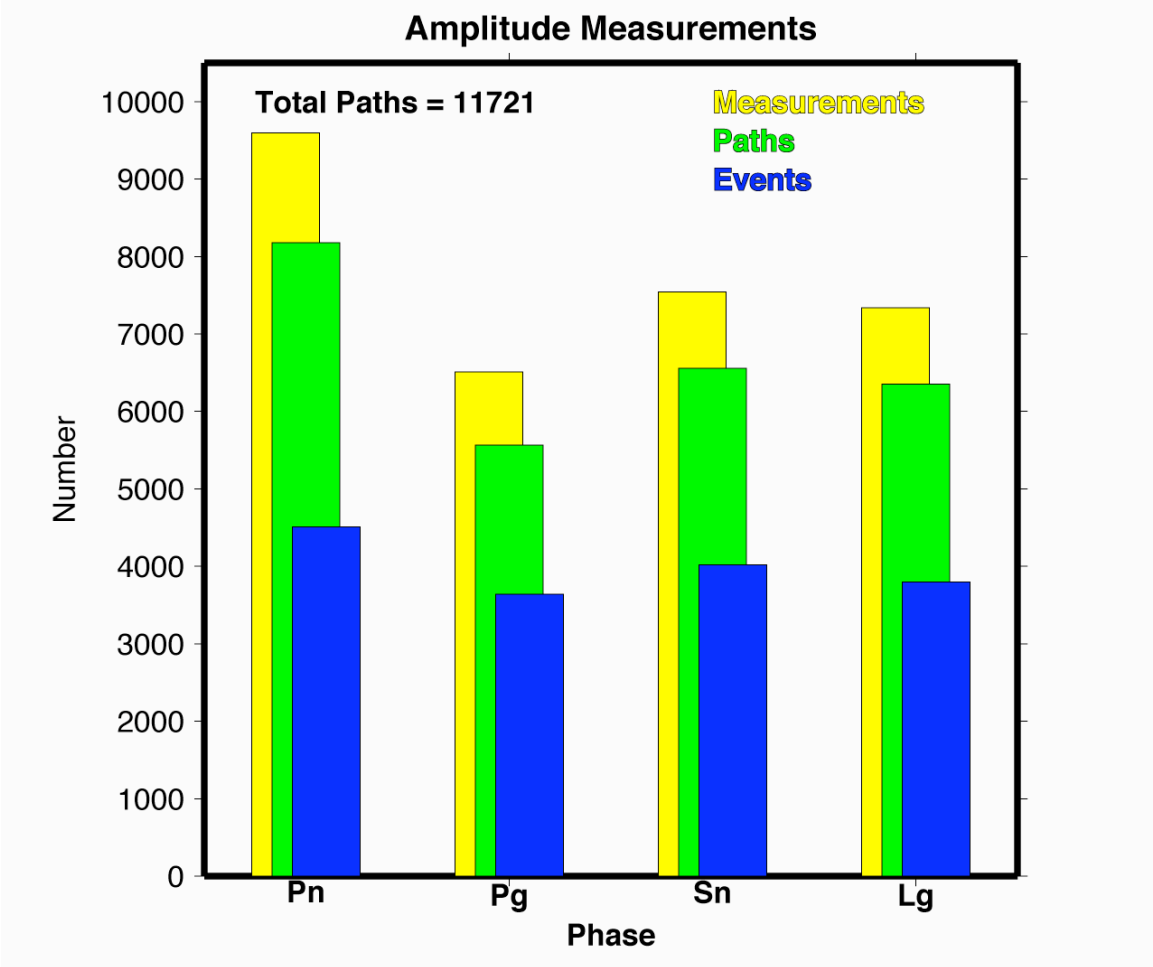
Amplitude Measurements
Total Paths = 11721
Measurements
Paths
Events
Number
10000
9000
8000
7000
6000
5000
4000
3000
2000
1000
0
Pn
Pg
Sn
Lg
Phase

Figure 2.

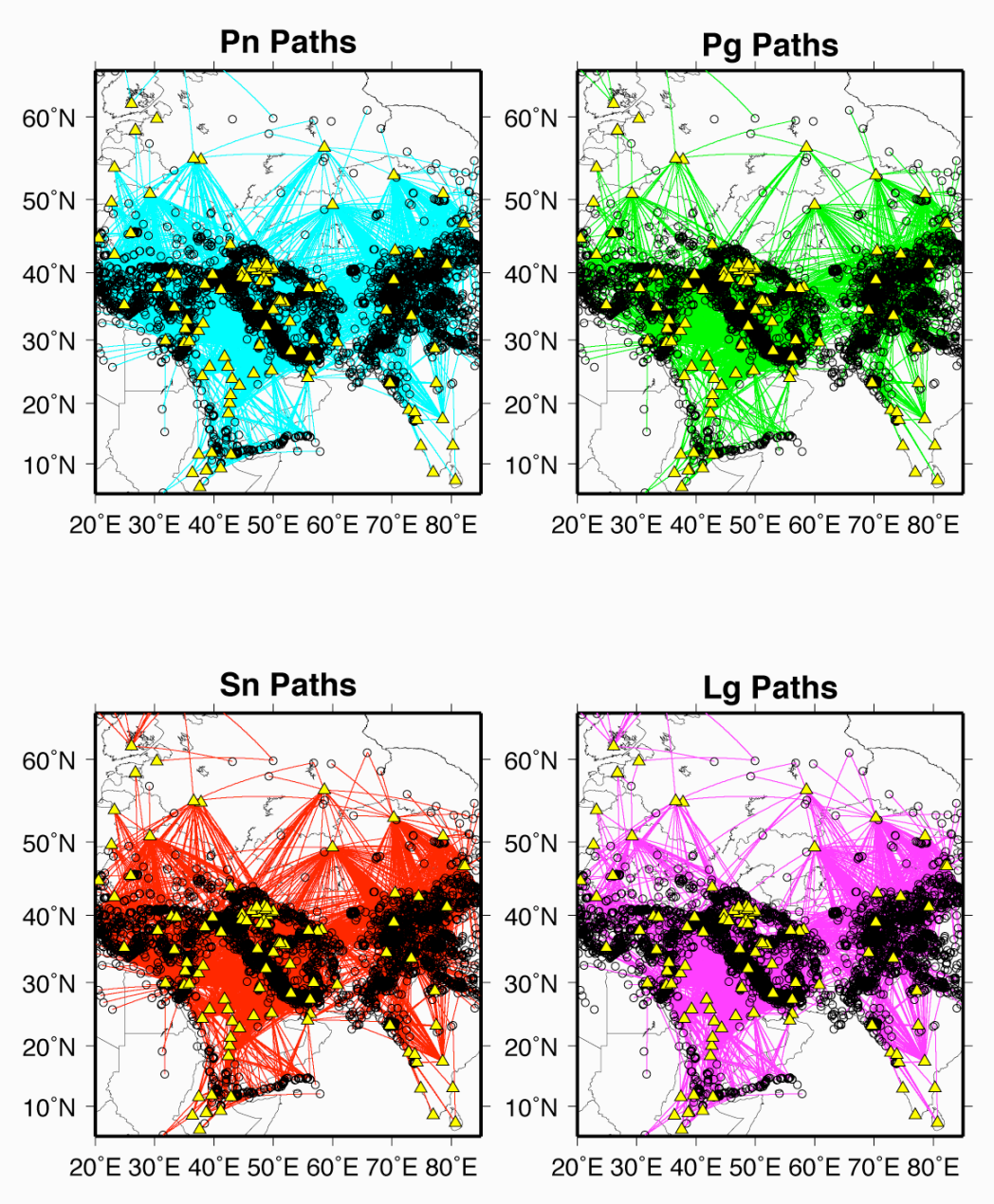
Pn Paths
Pg Paths
Sn Paths
Lg Paths
60°N
50°N
40°N
30°N
20°N
10°N
20°E 30°E 40°E 50°E 60°E 70°E 80°E

Figure 3.

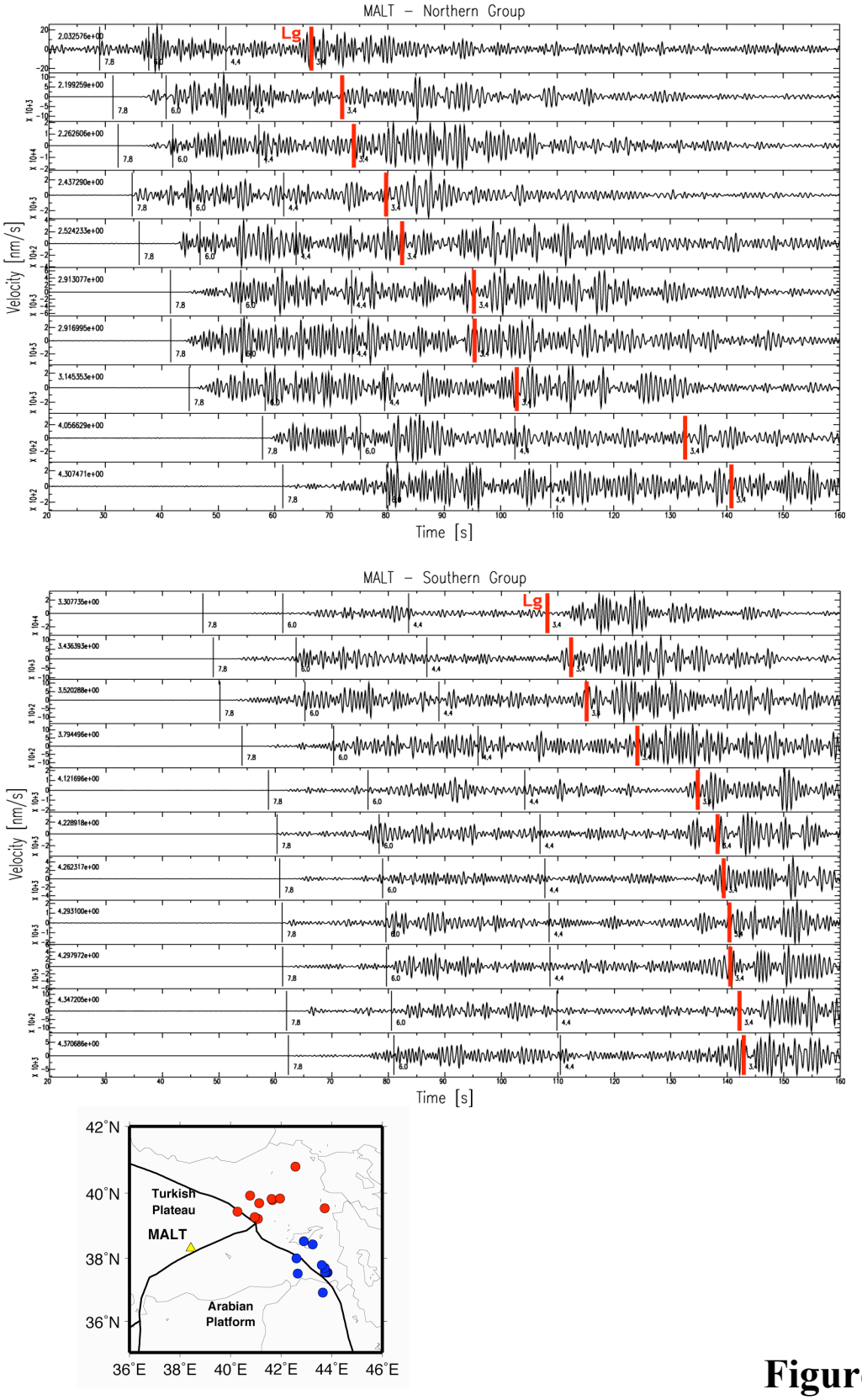
MALT – Northern Group
Lg
Velocity [nm/s]
Time [s]
MALT – Southern Group
Lg
Velocity [nm/s]
Time [s]
42°N
40°N
38°N
36°N
36°E
38°E
40°E
42°E
44°E
46°E
Turkish Plateau
MALT
Arabian Platform

Figure 4.

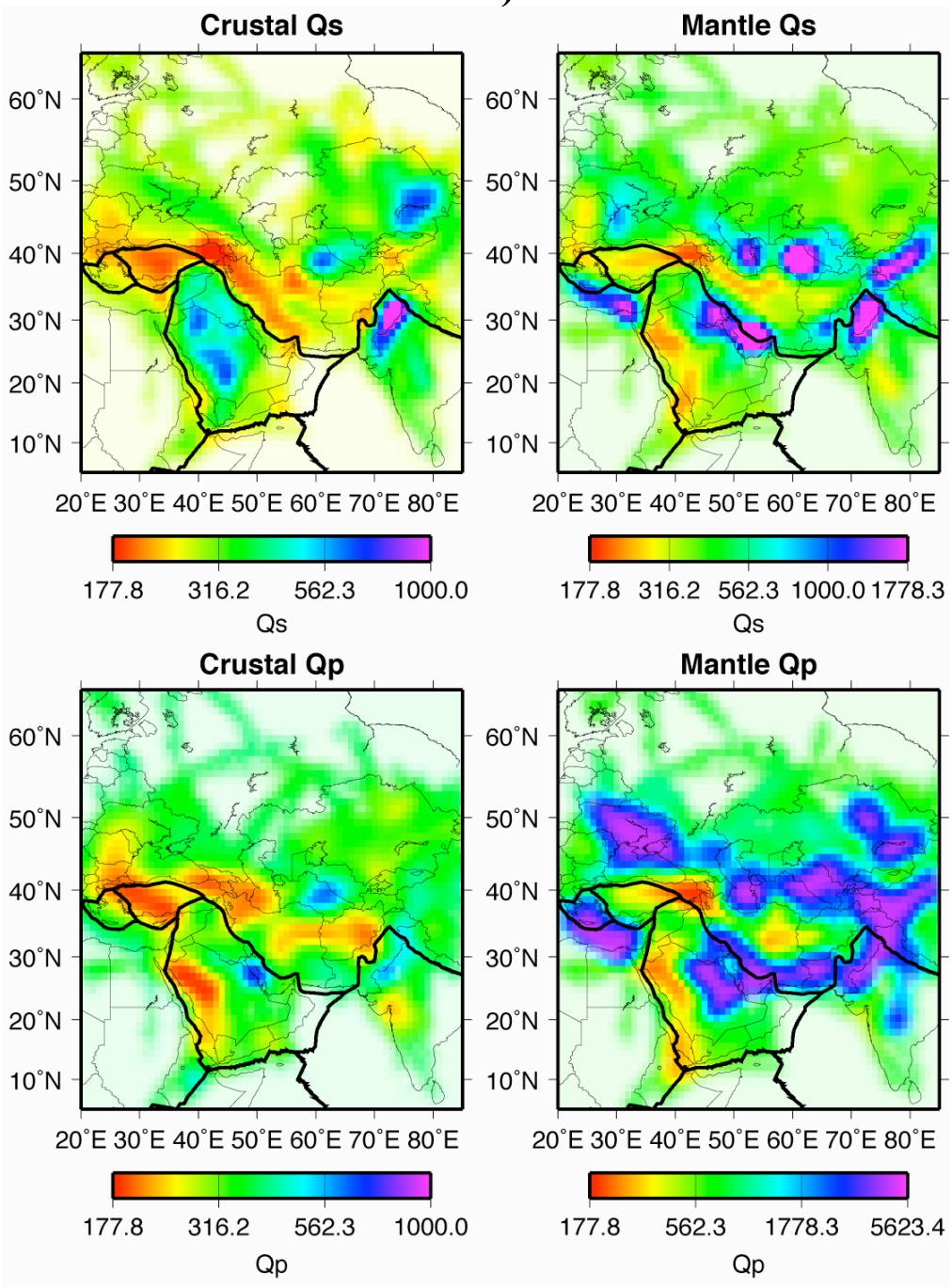
a)
b)
Crustal Qs
Mantle Qs
60°N
50°N
40°N
30°N
20°N
10°N
20°E 30°E 40°E 50°E 60°E 70°E 80°E
177.8 316.2 562.3 1000.0
Qs
177.8 316.2 562.3 1000.0 1778.3
Qs
Crustal Qp
Mantle Qp
177.8 316.2 562.3 1000.0
Qp
177.8 562.3 1778.3 5623.4
Qp
c)
d)

Figure 5.

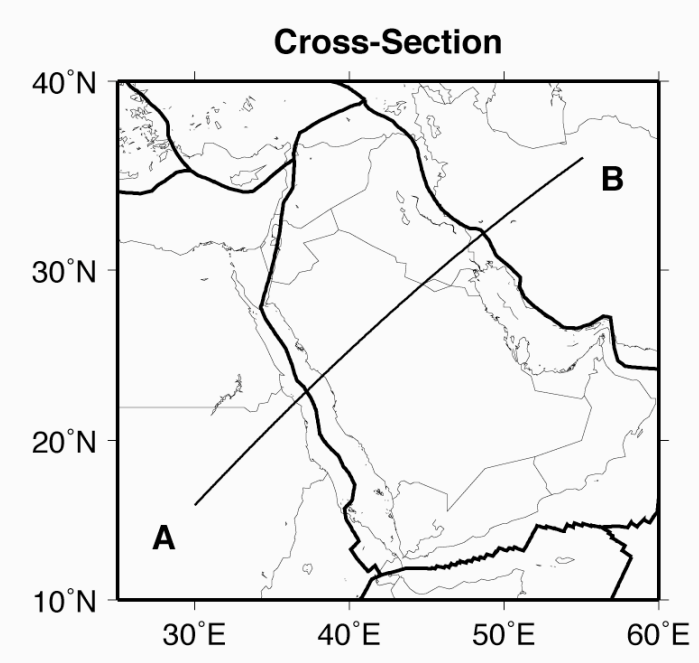
Cross-Section
40°N
30°N
20°N
10°N
30°E
40°E
50°E
60°E
A
B

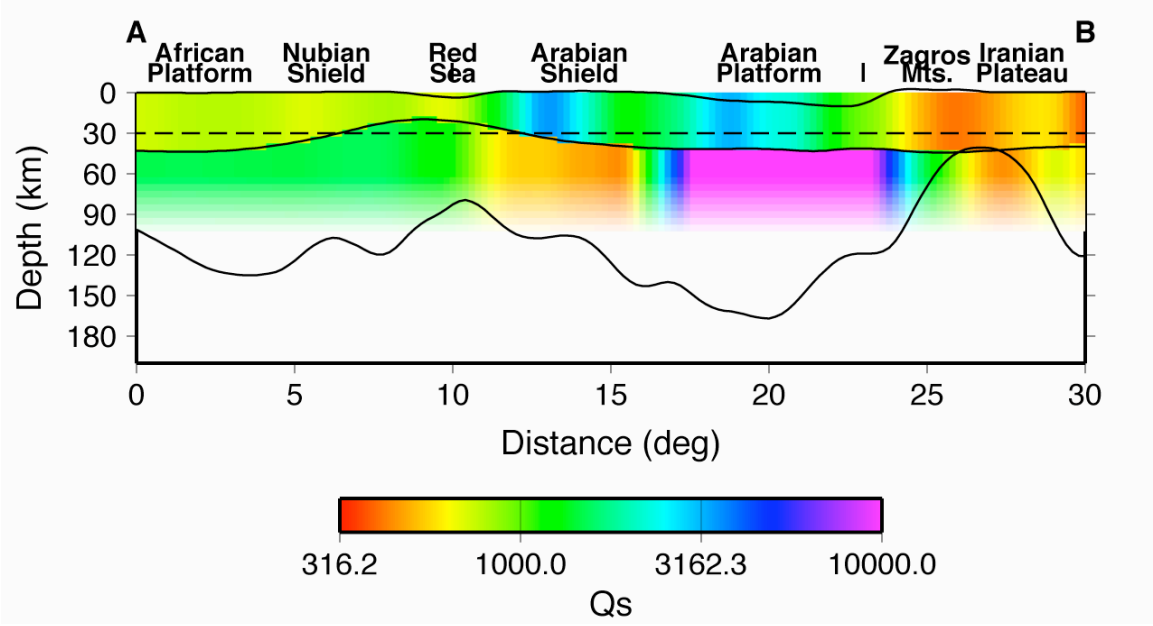
A
B
African Platform
Nubian Shield
Red Sea
Arabian Shield
Arabian Platform
Zagros Mts.
Iranian Plateau
Depth (km)
0
30
60
90
120
150
180
0
5
10
15
20
25
30
Distance (deg)
316.2
1000.0
3162.3
10000.0
Qs

Figure 6.

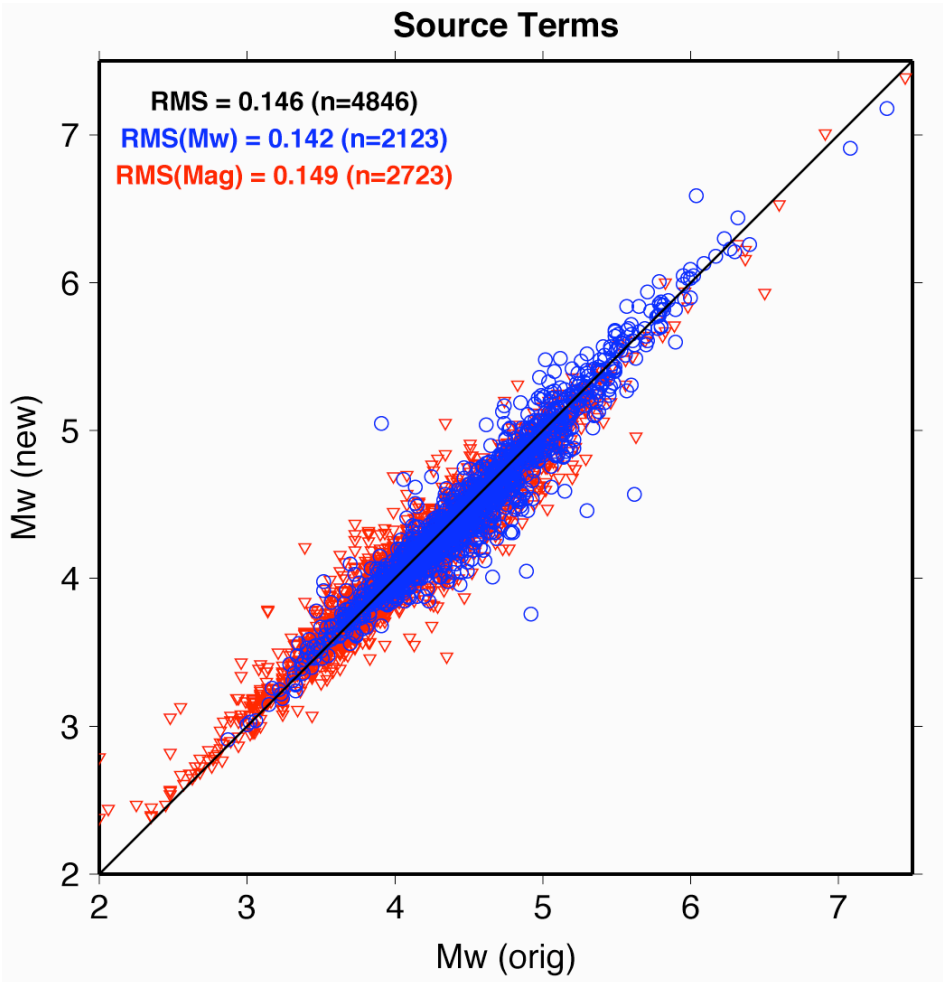
Source Terms
RMS = 0.146 (n=4846)
RMS(Mw) = 0.142 (n=2123)
RMS(Mag) = 0.149 (n=2723)
Mw (new)
Mw (orig)
2
3
4
5
6
7

Figure 7.

a) **b)**

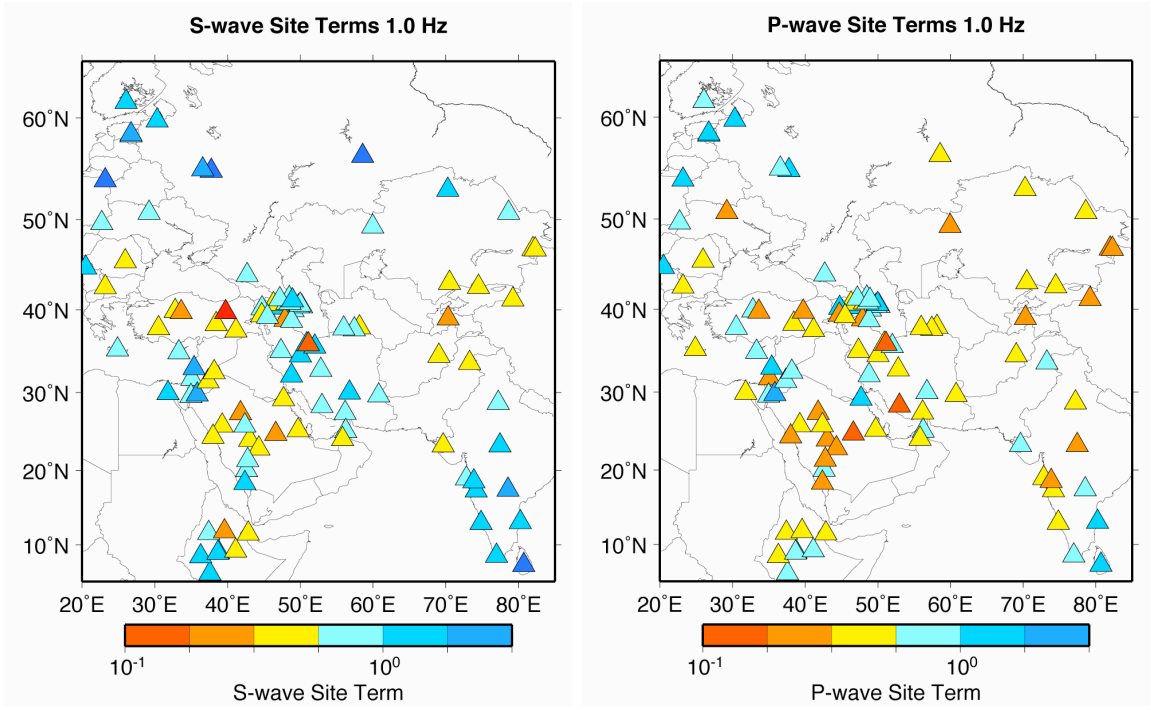
S-wave Site Terms 1.0 Hz
P-wave Site Terms 1.0 Hz
60°N
50°N
40°N
30°N
20°N
10°N
20°E
30°E
40°E
50°E
60°E
70°E
80°E
10-1
100
S-wave Site Term
P-wave Site Term

c)

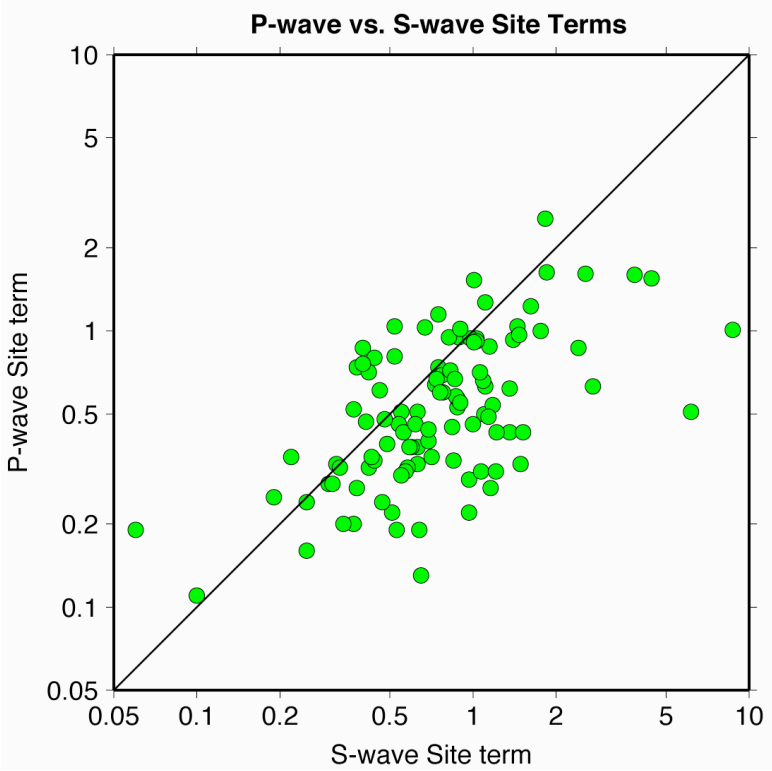
P-wave vs. S-wave Site Terms
P-wave Site term
S-wave Site term
10
5
2
1
0.5
0.2
0.1
0.05

Figure 8.

a)

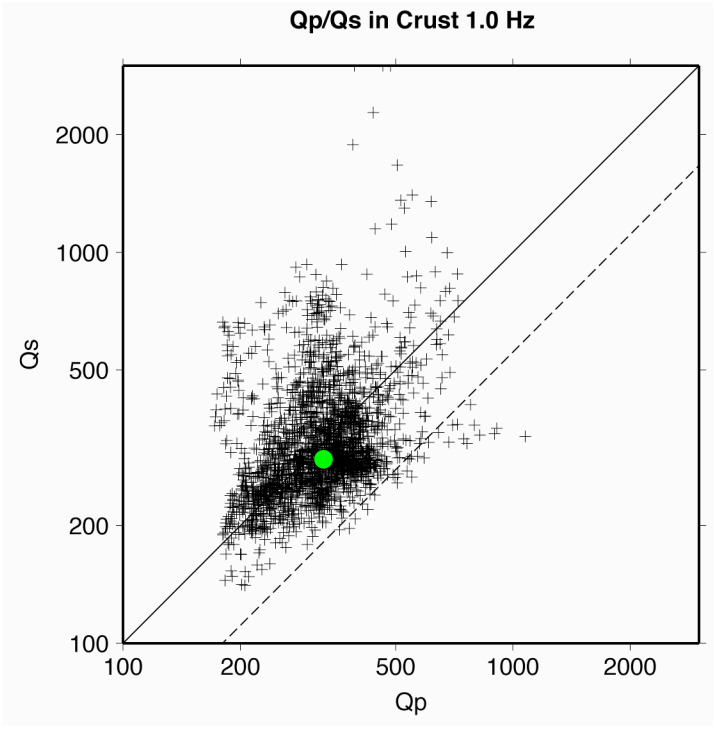
Qp/Qs in Crust 1.0 Hz
2000
1000
500
200
100
Qs
100
200
500
1000
2000
Qp

b)

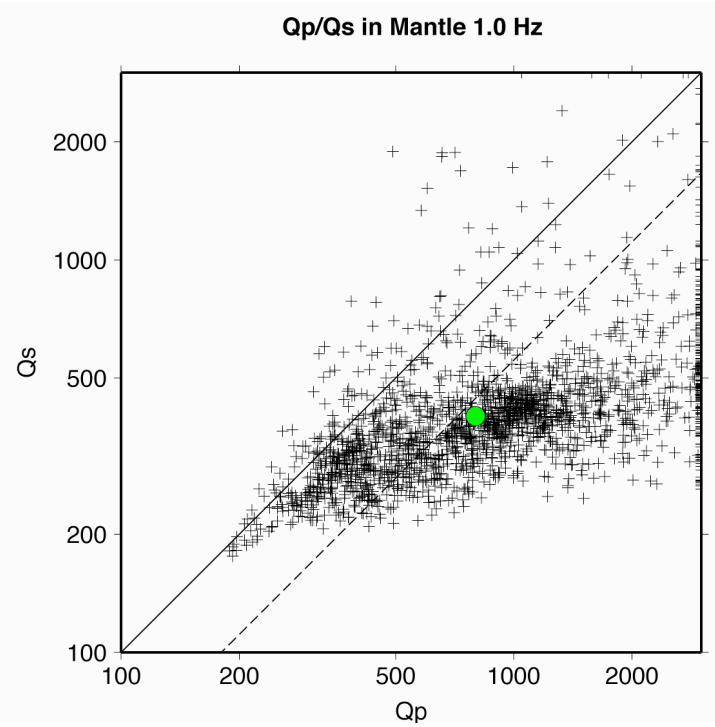
Qp/Qs in Mantle 1.0 Hz
2000
1000
500
200
100
Qs
100
200
500
1000
2000
Qp

Figure 9.